Quaternary Science Reviews 344 (2024) 108992

Contents lists available at ScienceDirect

Quaternary Science Reviews

journal homepage: www.elsevier.com/locate/quascirev

A 6000-year high-resolution composite record of El Niño-related drought in subtropical southeast Africa

Marc Humphries [a,*], Kei Prior [a], Andrew Green [b,c], Derrick Vaughn [d,e]

[a] School of Chemistry, University of the Witwatersrand, Johannesburg, South Africa
[b] Geological Sciences, University of KwaZulu-Natal, South Africa
[c] School of Geography and Environmental Sciences, Ulster University, Northern Ireland, UK
[d] School of the Environment, Yale University, USA
[e] Department of Geosciences, Utah State University, USA

ARTICLE INFO

Handling editor: P Rioual

Keywords:
ENSO
Aridity
Drought
Paleoclimate
Holocene
Southern africa

ABSTRACT

El Niño–Southern Oscillation (ENSO) extremes have a major impact on global temperature and rainfall patterns, triggering severe droughts and floods in many regions of the world. Paleoclimate records reveal significant changes in ENSO activity at centennial and millennial scales, but uncertainty remains regarding the exact nature of these variations during the Holocene and how they impacted climate patterns across different regions. Here we present a highly resolved sedimentary record from Lake Bhangazi North on the subtropical east coast of South Africa, where modern-day rainfall variability is profoundly influenced by ENSO through teleconnections mediated by the Walker Circulation. Stratigraphic and inorganic geochemical proxies at Lake Bhangazi North provide evidence for significant fluctuations in the local hydrological regime, characterised by extended intervals of aridity. Our findings corroborate independent sedimentary evidence from nearby sites at Lake Muzi and Mkhuze Delta, allowing for the generation of a composite proxy record of drought for the region. This record provides compelling evidence for the occurrence of several major drought events at ~5100–4200, 3600–2700, 1900–1700 and ~990 cal yr BP. The timing of these distinctive events exhibits striking correspondence with the ENSO proxy sedimentary record from Laguna Pallcacocha, Ecuador. We propose that El Niño, impacting moisture convergence over the subtropical eastern region of South Africa, was the primary driver of drought in the region over the mid-to-late Holocene. This hypothesis is further supported by stalagmite records from northwest Madagascar that reveal pronounced shifts towards wetter conditions coincident with major drought events in our study area, consistent with the modern rainfall anomaly pattern associated with ENSO. Our findings suggest that major aridity phases observed in records from the east coast of South Africa likely reflect large-scale shifts in regional moisture transport across subtropical southeastern Africa, driven by fluctuations in ENSO conditions.

1. Introduction

The El Niño-Southern Oscillation (ENSO) is a leading driver of interannual climate variability globally, exerting major influence on atmospheric and oceanic circulation patterns (Vecchi and Wittenberg, 2010). This cyclic phenomenon, characterised by warm (El Niño) and cool (La Niña) phases in the tropical Pacific, triggers a cascade of teleconnections that impact regions far beyond the Pacific basin itself. The subsequent changes in temperature and precipitation regimes can lead to increases in the frequency and intensity of extreme weather events, bringing severe droughts to some regions (e.g., Vicente-Serrano et al., 2011; Jiménez-Muñoz et al., 2016) and devastating floods to others (e.g., Ward et al., 2014). As one of the most prominent global modes of natural climate variability, ENSO is a critical target for investigations into the projected impacts of climate change.

While the influence of ENSO on global climate patterns is well-established, its specific impact on regional hydroclimate, particularly over long timescales, remains poorly understood due to a scarcity of high-resolution paleoclimate records and inherent complexities that arise from the nonlinear nature of the proxies used and the spatial heterogeneity of the climate system itself (Emile-Geay and Tingley, 2016; Emile-Geay et al., 2020). Furthermore, modern-day El Niño events display a diverse range of amplitudes, triggers and spatial patterns (Ashok et al., 2007; Capotondi et al., 2015), and therefore multiple

* Corresponding author.
E-mail address: marchump@gmail.com (M. Humphries).

https://doi.org/10.1016/j.quascirev.2024.108992
Received 31 July 2024; Received in revised form 1 October 2024; Accepted 2 October 2024
Available online 11 October 2024

records are critical for understanding the vast spatial scale associated with ENSO and its impact across diverse geographical regions. Such knowledge is crucial for understanding the mechanisms and influence of ENSO on extreme weather events around the world, and for mitigating the risks associated with a changing climate. Additional records from ENSO-affected regions are therefore needed to broaden our understanding of past ENSO variability at a global scale.

ENSO's influence on modern rainfall across southern Africa is well-documented (e.g., Reason and Rouault, 2002; Malherbe et al., 2016; Hoell and Cheng, 2018). El Niño events typically bring drier conditions and increased drought risk, while La Niña events are associated with enhanced rainfall and potential flooding (Washington and Preston, 2006; Hoell and Cheng, 2018). ENSO's influence on rainfall is mediated through regional circulation changes that affect moisture convergence and cloudband development over the central and eastern parts of the region, mainly during the summer rainfall season (Reason et al., 2000; Blamey et al., 2018). As a result, summer rainfall in southern Africa is characterised by a high degree of variability, with recurring cycles of drought and flood posing significant impacts on the region's water security, agricultural productivity, and biodiversity (Hao et al., 2020; Mathivha et al., 2024).

Given the robust relationship between ENSO and contemporary rainfall patterns across southern Africa, hydroclimate reconstructions from the region should integrate information on ENSO variability during periods of strong teleconnection. Previous work on the subtropical east coast of South Africa has shown that sedimentary records from coastal lakes and wetlands in the region provide hydrologically sensitive archives that record dramatic changes in Holocene hydroclimate (Humphries et al., 2016, 2019, 2020). The abrupt and large hydroclimate fluctuations captured in these records have been interpreted to reflect the impact of El Niño in the region. However, individual proxy records are inherently limited in their capacity to characterise regional conditions due to the influence of site-specific hydrological processes, the fidelity of the proxy in recording past environmental fluctuations, and uncertainties associated with the age-depth model.

Here, we present a new continuous and chronologically well-constrained sedimentary record from Lake Bhangazi North on the subtropical east coast of South Africa (Fig. 1). We interpret downcore variations in sediment stratigraphy, grain size and elemental composition to be driven by changes in sediment transport and deposition at the site that reflect climatically driven fluctuations in the local hydrological regime. We combine data from Lake Bhangazi North with previously

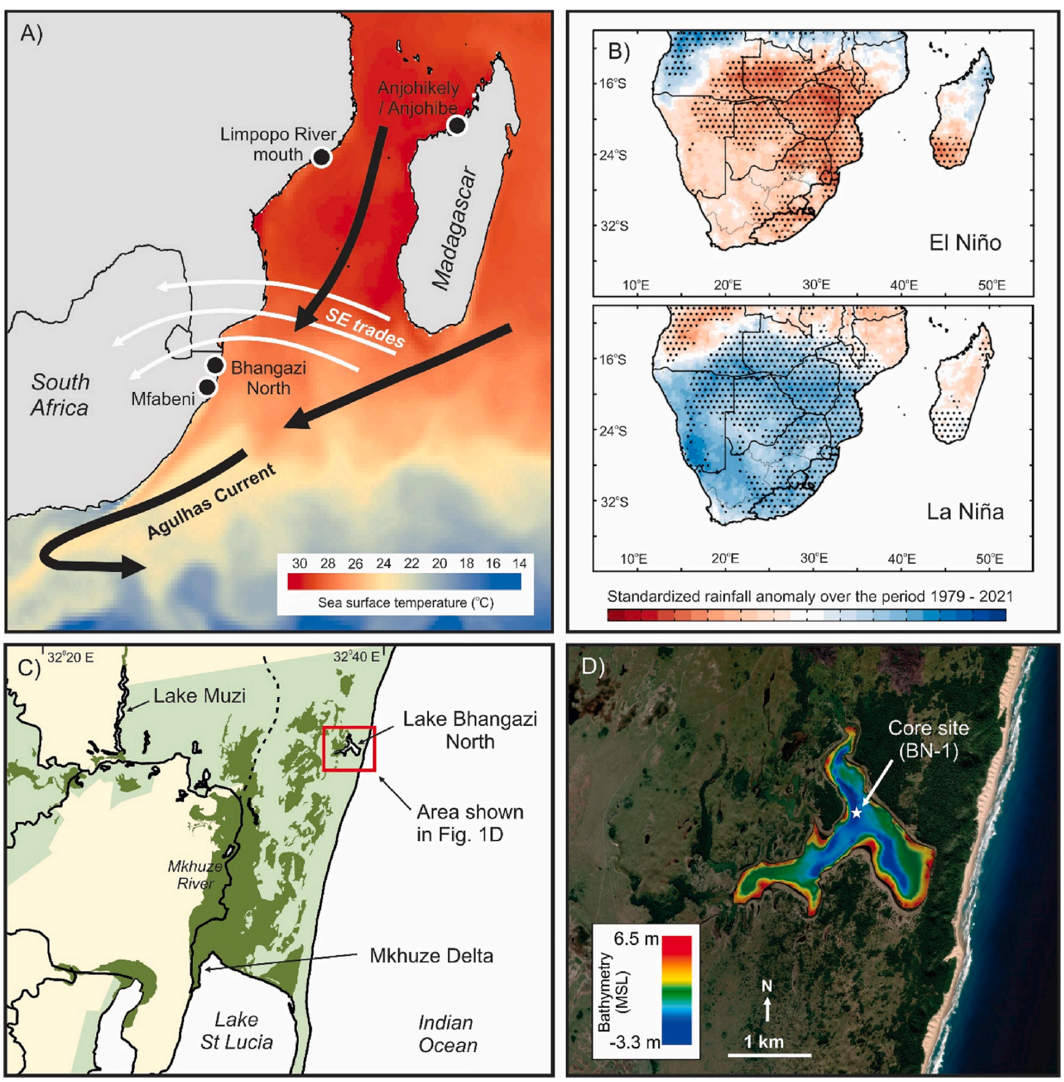

Fig. 1. A) Map of southeast Africa showing the major atmospheric and oceanic circulation systems that influence summer rainfall variability in the region. Average sea surface temperatures for January 2017 are shown (NASA GHRSST data). B) Summer (December–February) precipitation anomalies across southern Africa during El Niño and La Niña events over the 1979–2021 CE period. Stippling denotes values that are statistically significant at the 95% level (Blamey and Reason, 2023). C) The location of Lake Bhangazi North on the east coast of South Africa and other palaeoclimate records discussed in text. D) The location of core BN-1 retrieved from Lake Bhangazi North.

published high-resolution sedimentary evidence from Lake Muzi and Mkhuze Delta to generate a composite proxy record of drought for the region. The resultant composite record constrains the timing of major drought events in the region and provides new insights into the influence of ENSO in driving hydroclimate fluctuations in southeast Africa over the Holocene.

2. Regional settings

2.1. Modern climate

Lake Bhangazi North is a small (~2 km^2) freshwater lake situated on the Maputaland coastal plain (Fig. 1). The site lies within South Africa's summer rainfall region, receiving over 70% of its precipitation between October and March. Cloud bands, driven by intensified low-level convergence between the Angola Low and the South Indian High, are the primary contributors to summer rainfall (Hart et al., 2010, 2018; Manhique et al., 2011). This convergence zone defines the South Indian Ocean Convergence Zone (SICZ) and is sustained primarily by north-easterly moisture flux from the southwest Indian Ocean. Interannual variability in the strength and position of the SICZ, and thus cloud band development over southern Africa, has been strongly linked to ENSO (Lazenby et al., 2016; Hart et al., 2018). During strong El Niño events, the SICZ shifts north-eastward, disrupting Indian Ocean moisture supply and leading to characteristically dry summer conditions and increased drought risk across southern Africa. Conversely, La Niña events (negative ENSO phase) are typically associated with wetter than average conditions over much of southern Africa (Hart et al., 2010, 2018).

The regional precipitation response to ENSO is modulated by Indian Ocean sea surface temperature (SST) variability, manifested as a dipole pattern across the ocean basin via the Subtropical Indian Ocean Dipole (SIOD; Hoell et al., 2017). The SIOD modifies the flux of moisture over the central and eastern regions of southern Africa with warm (cool) SST anomalies over the tropical Indian Ocean and cool (warm) SST anomalies south of Madagascar associated with regionally dry (wet) conditions (Reason, 2002; Washington and Preston, 2006). Summer rainfall is thus impacted by the synchronous behaviours of ENSO and the SIOD, which act to modify the flux of moisture over the region and condition the probability of precipitation extremes (Hoell and Cheng, 2018). Historical observations and atmospheric model simulations show that summer precipitation anomalies tend to be amplified when ENSO and SIOD are in opposite phases (e.g. El Niño with negative SIOD or La Niña with positive SIOD; Fig. 1B). The probability of extreme dry summer rainfall seasons is thus significantly increased by El Niño, especially when combined with a negative SIOD (Washington and Preston, 2006; Hoell et al., 2017; Hoell and Cheng, 2018). While ENSO is primarily associated with summer rainfall patterns in southern Africa, observational evidence indicates a potential influence on austral winter rainfall cycles in the southwestern region of South Africa (Philippon et al., 2012).

2.2. Depositional setting

Lake Bhangazi North is an isolated freshwater system with no significant fluvial inputs. The lake is sustained primarily by groundwater flow through shallow coastal plain aquifers, with variations in lake level reflecting the local water table elevation. Like many of the coastal lakes in the region, the present-day system likely represents an incised valley that was back-flooded during the Holocene transgression (Botha et al., 2013; Wright, 2002). Dated sediment cores from the northern part of Lake St Lucia, located 30 km south of Bhangazi, indicate that coastal systems in the area likely become separated from the ocean around 7000 cal yr BP (Benallack et al., 2016; Humphries et al., 2020). Today, Lake Bhangazi North is sheltered from direct oceanic influences by an extensive (50–110 m high) vegetated, sandy Holocene-Pleistocene barrier.

The lake can be subdivided into a shallow western limb and a slightly deeper eastern limb that rests in the lee of the coastal dune complex. Bathymetric mapping indicates that the lake is dominated by a southwest-northeast trending channel that bifurcates into two channels aligned parallel with the coast (Ramdhunee, 2024). The deepest portions of the lake are associated with these channels, where relative depths of up to 9 m (−2.5 MSL) are found in the northern channel bifurcation.

3. Methods

3.1. Sampling

A 740 cm sediment core (BN-1) was retrieved from Lake Bhangazi North in January 2023. The coring site (Fig. 1) was selected following a bathymetric survey which identified a channel adjacent to the western bank to be the deepest point of the lake (Ramdhunee, 2024). The core was retrieved in ~8.9 m of water using a Uwitec barge-mounted piston corer. Core material was retrieved in contiguous 2 m sections (63 mm diameter liners) and transported to the laboratory where they were split longitudinally and described according to standard sedimentological procedures.

3.2. Chronology

Nine bulk sediment samples were selected for ^{14}C dating using accelerator mass spectrometry (AMS) Mini Carbon Dating System (MICADAS; IonPlus). Analyses were carried out at the Yale Analytical and Stable Isotope Centre (YASIC) at Yale University (USA). Sediment samples were immersed in 1 M HCl and placed in a 60 °C oven for 1 h. The acid was removed and the samples were rinsed with deionized and decarbonated water until the overlying rinse was neutral. The samples were then placed in a 60 °C oven to dry overnight.

Dry samples were weighed and packed into tin boats to be combusted on an elemental analyzer (EA) at 950 °C, which was coupled with an automated graphitization system (AGE-3; Ionplus AG; Wacker et al., 2010). Carbon dioxide from the EA was carried by a stream of helium to an adsorption trap (13X zeolite) and was converted through graphite using hydrogen gas as a reactant and iron powder (SIGMA ALDRICH; CAS: 7439-89-6) as a catalyst. Graphite samples were pressed into cathodes and these cathodes were inserted into a linear magazine holding up to 30 unknown samples, 3 normalization standards (NIST Oxalic Acid II (OxAII); NIST SRM4990C), 3 blanks (Phthalic Acid (PhA); Sigma Aldrich 320064, Lot # MKCN5082), and 3 secondary standards prepped with the unknown samples (IAEA-C7). Blank ages for combusted and graphitized samples ranged between 47 and 49 ^{14}C ka, similar to previously reported values for other MICADAS facilities (Bard et al., 2015; Mollenhauer et al., 2021; Cao et al., 2023). The values obtained for the standards ($F^{14}C$ = 1.3386–1.3423 and 0.4948–0.4965 for OxAII and IAEA-C7, respectively) were in agreement with reference values for the standards (reference $F^{14}C$ = 1.3407 and 0.4969 for OxAII and IAEA-C7, respectively). Radiocarbon data for the unknown samples was normalized and blank corrected against OxAII and PhA using BATS software version 3.6 (Wacker et al., 2010). Radiocarbon ages were calibrated using the Southern Hemisphere atmospheric curve SHCal.20 (Hogg et al., 2020, Table 1) and a Bayesian age-depth model was developed using Bacon 2.2 software (Blaauw and Christen, 2011, Fig. 2).

Table 1
Radiocarbon ages and calibration information for core BN-1.

Depth (cm)	14C age (yr BP)	95.4% probability range (cal yr BP)
21	1126 ± 17	1054–1020 (37.1%), 989–955 (45.1%)
85	1846 ± 18	1751–1698 (72.4%)
276	3228 ± 20	3450–3362 (95.4%)
370	3815 ± 20	4248–4080 (89.5%)
492	4878 ± 21	5605–5550 (48.9%), 5539–5477 (41.6%)
548	5285 ± 22	6027–5925 (55.8%), 6117–6042 (28.2%)
662	6586 ± 23	7514–7421 (84.8%)
694	6785 ± 23	7670–7569 (93.0%)
708	7141 ± 23	8010–7917 (62.2%), 7903–7850 (33.3%)

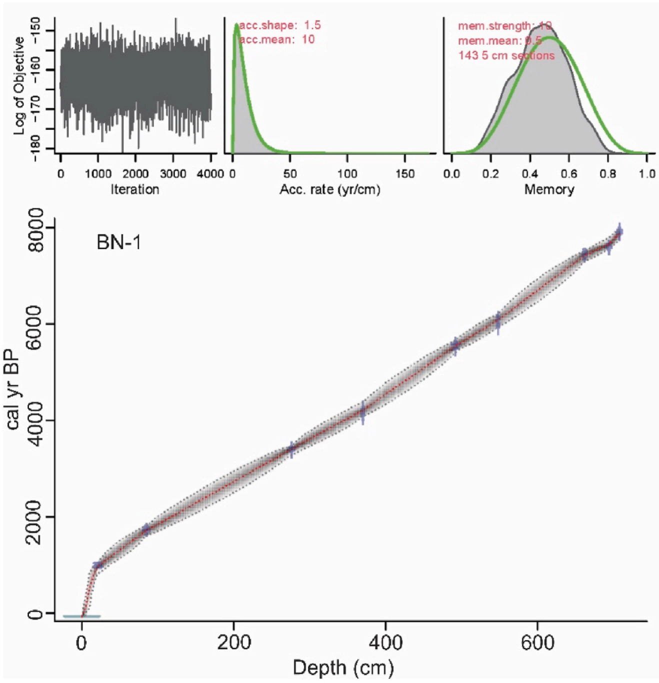

Fig. 2. Bayesian age-depth model for core BN-1 generated using the R package Bacon v2.5.8 (Blaauw and Christen, 2011). Top left panel: Markov Chain Monte Carlo iterations; top middle and right panels show the prior (green lines) and posterior densities (area fills) for the mean accumulation rate and memory, respectively. The large bottom panel shows the calibrated ^{14}C ages and the age-depth model. The central dotted line is the model based on the weighted mean age; grey shading represents the age model probability and contains the 95% confidence interval (dashed lines).

3.3. Sediment analyses

The core was subsampled at 2 cm intervals for geochemical analyses. Sediment samples were dried at 105 °C and milled to homogeneous powders, before being combusted at 550 °C for 4 h to estimate the proportion of organic by loss-on-ignition (LOI). Combusted powders were then analysed for major elements by X-ray fluorescence (XRF) using a Bruker S2 Ranger following calibration against a range of local and USGS rock standards. Internal precision of the analyses was always better than 2% for all elements based on the repeated analysis of USGS rock standards AVG-2 and GSP-2.

Grain size distributions were measured on subsamples taken at 14 cm intervals, ensuring that distinct changes in stratigraphy were captured. Samples were treated with 30% H_2O_2 and 10% HCl to remove organic matter and carbonates, respectively, and then suspended in 0.5% sodium hexametaphosphate to facilitate dispersion. The resulting suspension was analysed using a Malvern Mastersizer 2000.

3.4. Statistical methods

Cross-correlation analysis on time series data was carried out using the Palaeontological Statistics Software Package (PAST v 4.03). Regressions and change-point analysis were done using DataGraph 5.3.

4. Results

4.1. Core chronology and stratigraphy

The core extracted from Lake Bhangazi North appears to have captured the entire Holocene lacustrine infill, terminating in clean fine to medium grained sand that is characteristic of the surrounding coastal plain. Nine AMS age measurements yielded a coherent age-depth model for the core, indicating a basal age of ~8000 cal yr BP (Table 1; Fig. 2). All age determinations were stratigraphically consistent and reveal a fairly constant rate of sedimentary infill. The mean sedimentation rate for the record is 0.12 cm yr^{-1}, giving the XRF analyses a sample resolution of between 15 and 20 years.

The sedimentary succession is visually fairly homogeneous in nature (Fig. 3), consisting predominantly of dark brown, organic-rich mud (gytjja). The most prominent stratigraphic features are discrete sand lenses, which are distributed sporadically within the gytjja matrix. These sand layers typically vary from 3 to 5 mm thick, the most prominent of which are found between 5100 and 4600, 3500–3200, 2000–1700 and 980–880 cal yr BP. The upper gytjja-dominated section of the profile is underlain by cohesive clayey material, which terminates in fine-medium clean sand at a core depth of ~710 cm.

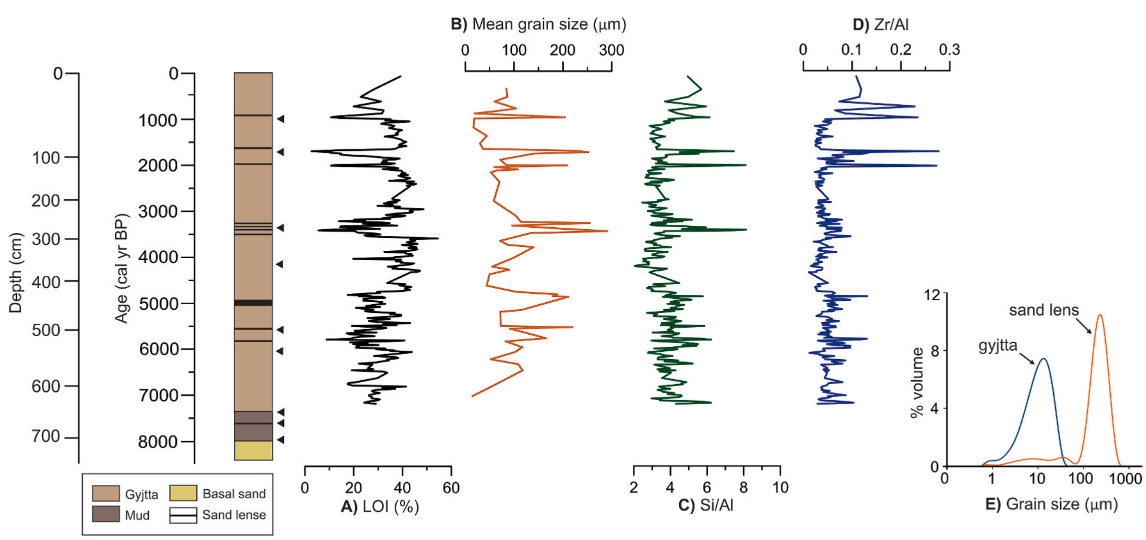

Fig. 3. Lithology of core BN-1 plotted alongside downcore variations in key physical and geochemical indicators (A–D). Representative grain size distributions showing the fine-grained sediment component associated with gyjtta and aeolian-derived sand lenses (E). Radiocarbon age control points are noted with black triangles.

4.2. Sediment composition

Sediment analyses reveal distinct downcore fluctuations in mean grain size and chemical composition (Fig. 3A–D). The most prominent peaks in grain size correspond with visually distinct sandy lenses and grain size distributions reveal the presence of two distinct sediment types. Gyjtta is characterised by relatively fine particles, with a mode of around 15–20 μm, while sand lenses have a modal size of ~270 μm (Fig. 3E) that is characteristic of dune sand in the region (Humphries et al., 2017). Increases in grain size show corresponding increases in Si/Al and Zr/Al ratios, which points to marked changes in sediment source and depositional conditions over time. Enrichments in Si correspond with the quartz-rich composition of the sand lenses, while Zr reflects the presence of zircon, a heavy mineral commonly associated with coastal sands in northern KwaZulu-Natal (Humphries et al., 2020).

5. Discussion

5.1. Proxy interpretation

Lake Bhangazi North is sheltered behind a 50–110 m high vegetated barrier that originated in the Pleistocene, and like many of the coastal systems in the region (e.g., Wright, 2002; Botha et al., 2013), the modern system likely represents an incised valley that was back-flooded during the Holocene transgression. The abrupt transition from fine-to medium-grained sands to mud-dominated sediments within core BN-1 indicates a distinct environmental shift that is interpreted as marking the onset of lacustrine conditions around 8000 cal yr BP. The subsequent deposition of predominately organic-rich sediments, devoid of shell material, is indicative of a sustained, tranquil lacustrine environment following marine disconnection. However, interspersed within this matrix is the presence of discrete sand lenses that represent the input of coarser material enriched in heavy minerals into the lake. These layers mark distinct shifts in sediment provenance and depositional mechanism over time, which we interpret to reflect episodic influxes of locally derived, aeolian sand into the lacustrine environment. There are several possible mechanisms through which coarse sediment can be mobilised, such as intensified wind strength, increased erodibility due to vegetation disturbance, and temporal fluctuations in local sediment sources driven by changes in the hydrological regime. At Lake Bhangazi, we consider enhanced aeolian deflation to most likely be a reflection of changes in hydroclimate, with prolonged arid phases exposing previously submerged lake shorelines and increasing the availability of erodible sediment. Variations in the sedimentary composition of BN-1 are thus interpreted to reflect the combined influence of sediment provenance and the prevailing transport mechanism, mediated primarily by fluctuations in regional hydrological conditions. Considering Lake Bhangazi North is sustained primarily by groundwater flow via an extensive coastal plain aquifer, lake levels are likely to be relatively insensitive to short-term fluctuations in hydrological conditions. Consequently, the episodic influx of aeolian sand into the system is likely to correspond with prolonged periods of drought.

5.2. Regional climatic reconstruction

The sedimentological and geochemical variations revealed in sediments from Lake Bhangazi North provide evidence for abrupt shifts in hydroclimate to markedly drier conditions at 5100–4600, 3500–3200, 2000–1700 and 980–880 cal yr BP. The timing of these shifts is broadly consistent with proxy evidence recorded in sedimentary sequences from Lake Muzi (Humphries et al., 2019) and Mkhuze Delta (Humphries et al., 2020, Fig. 4B and C). These two sites are located 20–30 km from Lake Bhangazi but represent very different settings in the landscape. Muzi is a small (2.9 km^2) freshwater lake situated on the Mkhuze River floodplain (Fig. 1C). The system represents a blocked-valley lake, sustained primarily by a combination of groundwater flow and occasional overspill from the Mkhuze River during high flow events. Hydroclimatic variability at this site is recorded in distinct shifts between the supply of fluvial sediment during relatively wet periods and the *in situ* precipitation of thick calcium carbonate units (indicated by Ca/K) during periods of prolonged aridity (Humphries et al., 2019). In contrast, the Mkhuze record represents a predominately fluvial sequence from a contemporary bayhead delta that discharges into the northern-most part of the St Lucia estuarine system (Fig. 1C). At this site, coarsening in grain size and heavy mineral enrichment (indicated by Zr/Al) are linked to aeolian influx of dune sand during periods of aridity. This pattern is similarly reflected in the enrichment of Sr (indicated by Sr/Al) which is linked to the presence of shell debris layers, interpreted to reflect mass mortality events among estuarine molluscs triggered by prolonged periods of hypersalinity or desiccation (Humphries et al., 2020).

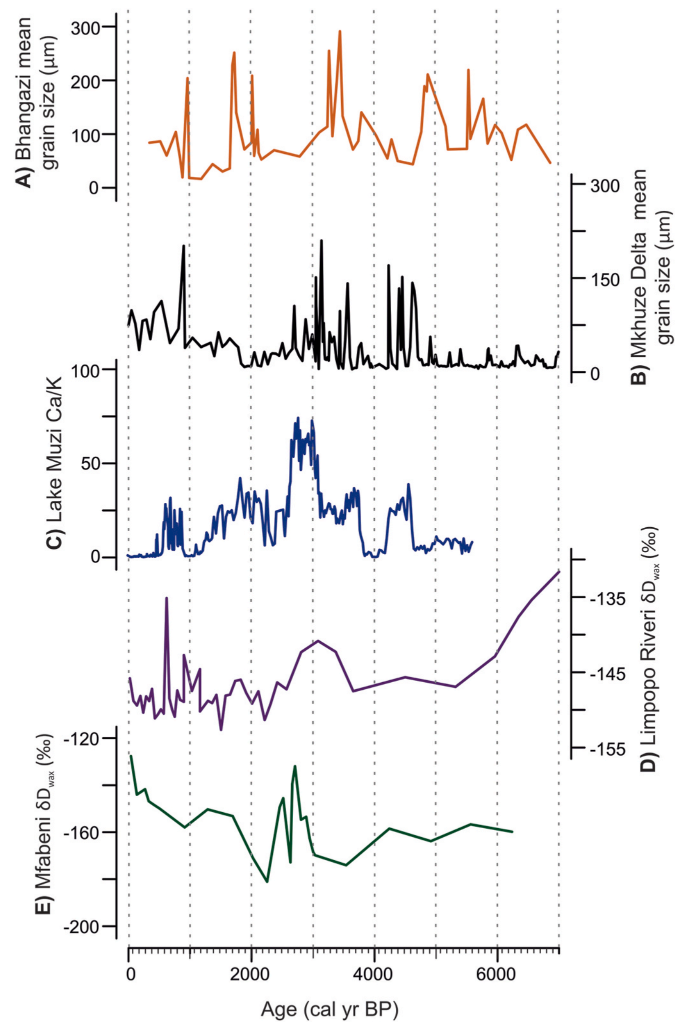

Fig. 4. Comparison of proxy records considered in this study. A) Variations in mean grain size through core BN-1 (this study). B) Variations in mean grain size through core MKD1 (Humphries et al., 2020). C) Lake Muzi (Humphries et al., 2019). D) δDwax record from the Limpopo River delta (Miller et al., 2020). E) δDwax record from Mfabeni peatland (Miller et al., 2019). Axes plotted to indicate dry conditions as upwards.

Given the differing sensitivities of these individual sites to changes in water availability, the nonlinear relationships between proxies and environmental conditions, and inherent errors associated with age-models, subtle differences in the timing and magnitude of aridity signals between records is not surprising. Rather than examining such subtle differences, we focus on identifying the most prominent periods of significant hydroclimatic fluctuation. The four distinct shifts to drier conditions identified in the Bhangazi record broadly align with similar fluctuations found in the Muzi and Mkhuze records, although not all events are captured at each location (Fig. 4). For example, the dry period at Lake Bhangazi 2000–1700 cal yr BP is reflected in the Muzi geochemistry record but seemingly not at Mkhuze. Nevertheless, when considered together, the broad trends revealed by the sedimentary records from Bhangazi, Muzi and Mkhuze provide compelling evidence for the occurrence of a series of protracted drought events along the east coast of South Africa over the last 6000 years.

While high-resolution records from Lake Muzi and Mkhuze Delta provide the most temporally congruent data for comparison with BN-1, δDwax data from the Limpopo River mouth (Fig. 4D; Miller et al., 2020) and Mfabeni Peatland (Fig. 4E; Miller et al., 2019) offer supporting evidence for large amplitude changes in moisture availability along the east coast of southern Africa, albeit at a lower resolution. At Mfabeni, a shift to markedly drier conditions is recorded at 3000–2500 cal yr BP, with a similar shift observed in the Limpopo record at 3800–2500 cal yr BP. The timing of these shifts corresponds well with what appears to be the most prolonged period of drought (3800–2600 cal yr BP) evident in the records from Bhangazi, Mkhuze and Muzi.

5.3. Drivers of drought in the region

Records from the eastern coastline of South Africa reveal a history of drought events in the region. These events have previously been interpreted to reflect primarily the influence of El Niño on tropical-moisture convergence and rainfall in eastern South Africa (Humphries et al., 2019, 2020). The new record from Lake Bhangazi North provides an opportunity to test this hypothesis more robustly. A single site can only inform on local conditions and is subject to limitations associated with the sensitivity of the hydrological setting, the reliability of the proxy record in capturing past environmental events, and age model uncertainties. To construct a regional-scale aridity history, aridity proxies from Lake Bhangazi, Lake Muzi and Mkhuze Delta (shown in Fig. 4) were normalized using z-scores, interpolated to a common resolution (25 years), and summed to generate a composite record (Fig. 5A). The resulting composite record should minimize the influence of site-specific biases and uncertainties associated with individual chronologies, and therefore provide a more robust reconstruction of the broader-scale climatic pattern. Mfabeni and Limpopo River are excluded in the generation of this record due to the relatively low resolution of these proxy data sets over the time period under consideration here.

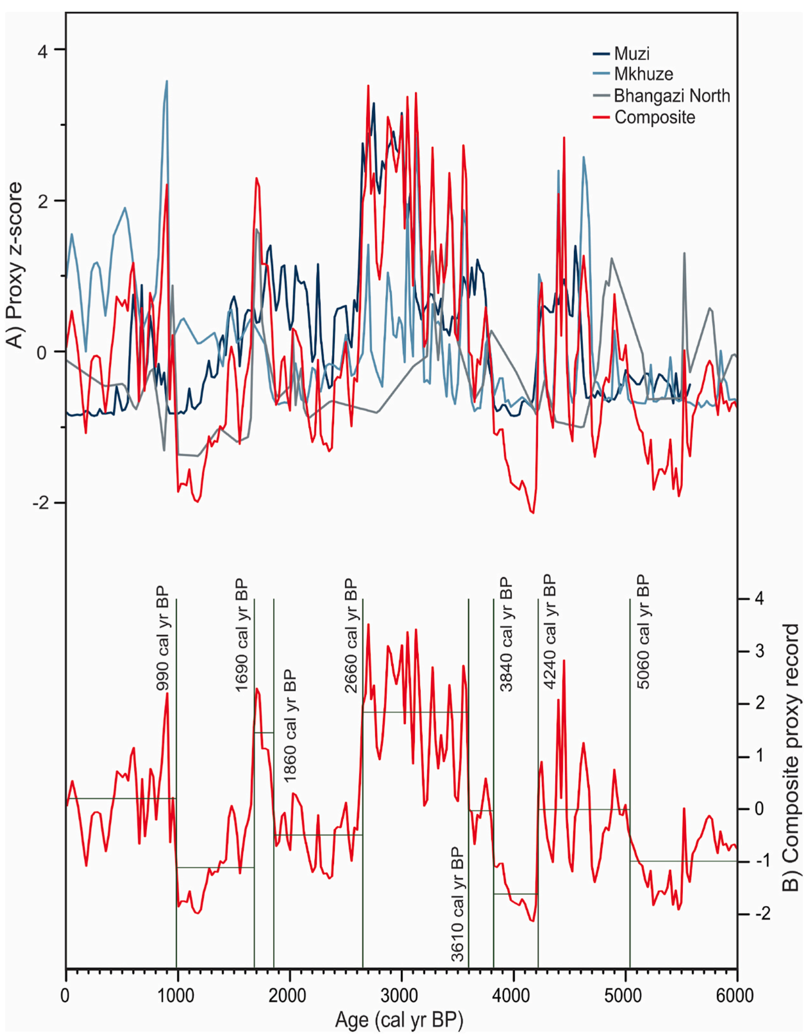

Fig. 5. The drought composite record developed for the east coast of South Africa. (A) The individual records used to generate the proxy composite are shown overlaid; Lake Muzi (Humphries et al., 2019), Mkhuze Delta (Humphries et al., 2020) and Lake Bhangazi North (this study). All records were interpolated to a common resolution of 25 years and the composite generated by merging z-score aridity proxy values. B) Results of change point analysis indicating the most significant changes in mean values in the composite record.

The generated composite record provides evidence for the occurrence of several major drought events (Fig. 5B). Change point detection (abrupt changes in the mean) indicates several significant shifts in moisture availability with prominent periods of aridity occurring at 5060–4240, 3610–2660, 1860–1690 and ~990 cal yr BP. The timing of these events exhibit remarkable correspondence with signals recorded in the sedimentary sequence from Laguna Pallcacocha, Ecuador (Fig. 6–Moy et al., 2002), perhaps the single most iconic record of Holocene ENSO variability. The laminated sediments preserved at Laguna Pallcacocha are considered to reflect flood and run-off variations associated with El Niño-driven convective storms. Although there has been some debate regarding the proxy interpretation of this record (see Kiefer and Karamperidou, 2019), comparison of recent debris flow deposition with historically documented El Niño events have confirmed that flood-driven clastic deposition at the site is closely tied to El Niño event frequency (Hagemans et al., 2021; Mark et al., 2022).

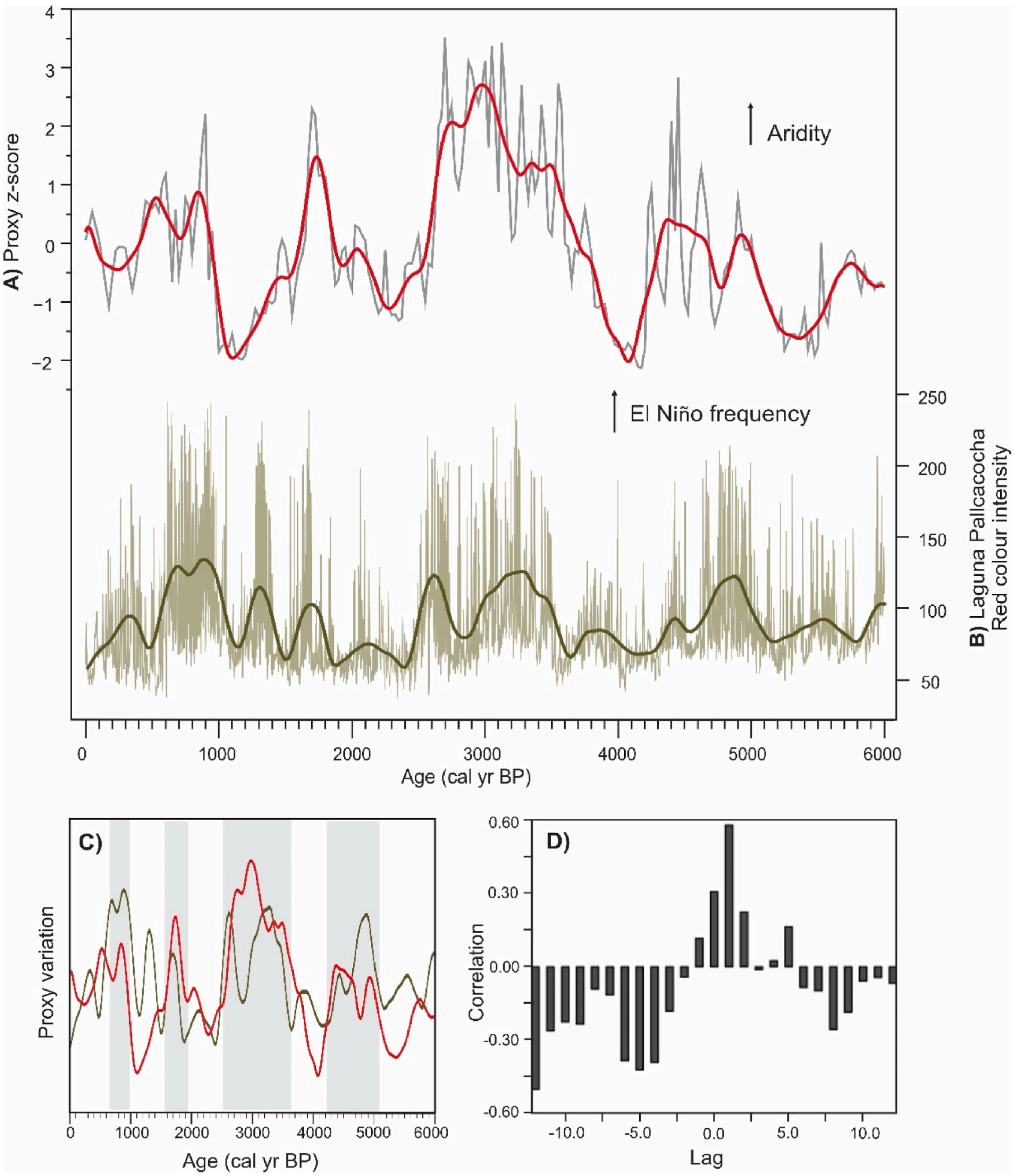

Fig. 6. Comparison between A) the composite drought record developed for the subtropical east coast of South Africa (this study) and B) ENSO proxy record from Laguna Pallcacocha, Ecuador (Moy et al., 2002). Dark lines indicate LOESS smoothing using a 250-year window. C) Overlay of the 250-year trends captured in the composite drought record and in El Niño activity at Laguna Pallcacocha. Vertical shaded lines indicate overlap between prominent periods of aridity in the composite record (as defined by change-point analysis; Fig. 6B) and increased El Niño activity at Laguna Pallcacocha. The cross-correlation between these two time series signals is shown in panel D.

Marked parallels are evident between our composite drought record and El Niño activity at Laguna Pallcacocha at multi-centennial to millennial timescales (Fig. 6), with periods of increased El Niño frequency corresponding well with inferred periods of drought. Statistical analysis of this relationship yielded a significant cross-correlation coefficient of 0.58 ($p = 0.004$) over a 250-year interval. This shared pattern of variability suggests that our composite drought record likely captures the most prominent, low-frequency features associated with ENSO activity over the last 6000 years. The most notable discrepancy occurs between ~1300 and 1400 cal yr BP, where the two records appear to be out-of-phase.

Although proxy records from the tropical Pacific indicate persistent and substantial shifts in ENSO variability through the mid-to-late Holocene, it is worth noting inconsistencies between sedimentary records purported to reflect ENSO (see, for example, Rein et al., 2005; Zhang et al., 2014). Given the inherent complexities of attributing flood deposits to El Niño events and the variable sensitivity of sedimentary archives to flood magnitude, such discrepancies are not surprising. Further complicating this picture is the spatial heterogeneity of ENSO events, or ENSO "flavours", which arise from contrasting spatial patterns of SST anomalies during El Niño, leading to differential hydroclimatic impacts across the Pacific basin (Karamperidou et al., 2015; Kiefer and Karamperidou, 2019). Eastern Pacific events are accompanied by strong warm SST anomalies and an increase in precipitation in the eastern Pacific, while Central Pacific events are associated with weaker SST anomalies that lead to heterogeneous impacts on local precipitation (Capotondi et al., 2015). Thus, seemingly contradictory Holocene records could be explained by changes related to ENSO diversity and the associated hydroclimatic teleconnections through time (Karamperidou and DiNezio, 2022).

Analysis of surface sediment indicates that clastic layers in Laguna Pallcacocha most likely record eastern Pacific El Niño events (Hagemans et al., 2021), as well as “mixed” El Niño when both eastern Pacific and Central Pacific flavours occur in the same event (Mark et al., 2022). The co-variation observed between flood events recorded at Laguna Pallcacocha and our composite drought record thus appears to signify a potential long-term teleconnection between ENSO-like variability and hydroclimate in the region over multi-millennial timescales.

5.4. Regional climatic context

Given the statistically robust relationship between the Pallcacocha record and drought events along the eastern margin of subtropical South Africa, we would expect to find corroborative evidence of hydroclimatic teleconnections across the region. The Mkhuze River, a major source of water at the Muzi and Mkhuze sites, and a possible contributor to groundwater at Lake Bhangazi, originates ~125 km inland and drains a catchment area of 5000 km^2. The hydrological signals recorded at our three sites thus likely integrate conditions over a much larger area than the immediate coastal environment.

To explore the spatiotemporal influence of El Niño on the southwestern Indian Ocean sector in more detail, we compare our composite drought record with high-resolution speleothem data from northwest Madagascar. An antiphase relationship exists between ENSO and modern day climate in southern Africa and northwest Madagascar (Jury et al., 1995, Fig. 1B). This reversal is attributed to the position of the Walker circulation cell in the southern Indian Ocean during El Niño, which has a subsiding limb over southern Africa and a rising limb over Madagascar (Lindesay, 1988). Stalagmite stable isotope records from Anjohibe (Wang et al., 2019) and Anjohikely (Scroxton et al., 2023) provide evidence for significant and abrupt changes in the hydroclimate of northwest Madagascar over the mid-to-late Holocene (Fig. 7). While there are some discrepancies between these records (see Scroxton et al., 2023 for a detailed discussion), anomalies observed in both data sets point to multiple hydroclimatic fluctuations likely linked to broader-scale climate change in the region. These include a shift from relatively wet conditions 4700–4400 cal yr BP to significantly dry conditions (indicated by the hiatus in both records) 4300–3900 cal yr BP. This shift appears to mirror hydroclimatic changes that occurred along the east coast of South Africa. Similarly, a strong shift to wetter conditions ~2700 cal yr BP, most notable in the Anjohikely record, coincides with particularly prolonged arid phase along the eastern South African coast. Overall, correspondence in hydroclimate shifts identified in stalagmite records from northwest Madagascar points to an antiphase relationship in moisture originating from the Indian Ocean that is consistent with an ENSO driver.

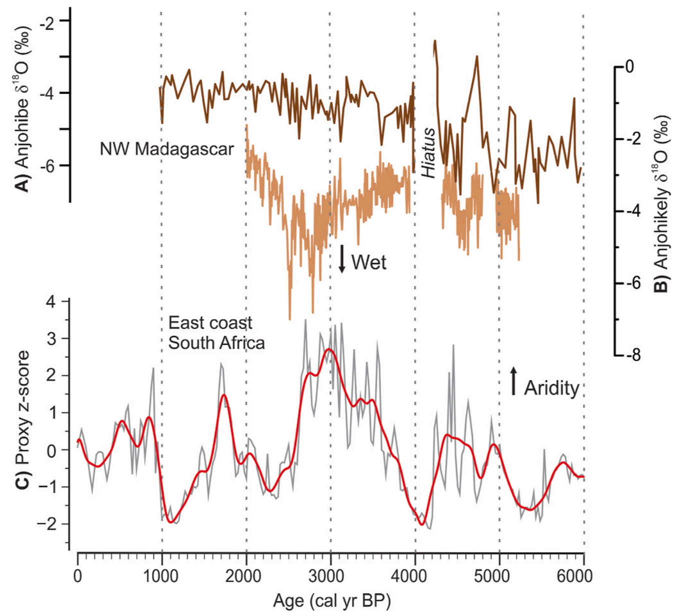

Fig. 7. Comparison between stalagmite proxy evidence from northwest Madagascar, A) Anjohibe Cave (Wang et al., 2019), and B) Anjohikely Cave (Scroxton et al., 2023), with C) the composite drought record developed from sedimentary sequences along the subtropical east coast of South Africa (this study).

6. Conclusions

The record from Lake Bhangazi North provides new high-resolution proxy evidence for the occurrence of several major drought events in eastern South Africa over the last 6000 years. These findings corroborate independent sedimentary evidence from Lake Muzi and the Mkhuze Delta, yielding a unique dataset that facilitates the construction of a composite drought record for the region. The composite record provides compelling evidence for the occurrence of major drought events at 5060–4240, 3610–2660, 1860–1690 and ~990 cal yr BP. While climate in the region is potentially influenced by a variety of forcing mechanisms, correlation between phases of aridity and El Niño frequency at Laguna Pallcacocha suggests that changes in ENSO activity during the mid-to-late Holocene played an underlying role in triggering periods of exceptional drought along the subtropical coast of South Africa.

The drought reconstruction presented in this study relies on proxy data collected from coastal sites, which are strongly influenced by Indian Ocean moisture fluxes and heat transported by the Agulhas Current. This necessitates caution when extrapolating the findings to assess the full spatial extent of ENSO’s influence, which is known to exhibit regional variability across southern Africa. Nevertheless, close correspondence in the timing of substantial moisture fluctuations over eastern South Africa and northwest Madagascar suggests that our composite drought record may capture a regional hydroclimate signal tied to the most prominent, low-frequency features of ENSO.

Declaration of competing interest

The authors declare that they have no known competing financial interests or personal relationships that could have appeared to influence the work reported in this paper.

Data availability

Data will be made available on request.

Acknowledgements

The authors received no direct funding for this work. Field work and analysis costs were borne by AG and MH. Radiocarbon analyses were supported through the Blue Carbon Timescale Network (BCTN) at Yale University, which is funded through Yale's Center for Natural Carbon Capture. The work was carried out under research permits issued by KZN Ezemvelo Wildlife and the iSimangaliso Wetland Park Authority. We thank Diaksha Ramdunee and Samantha Halford for their assistance in the field, and Rachel Mey for assisting with some of the geochemical analyses.

Appendix A. Supplementary data

Supplementary data to this article can be found online at https://doi.org/10.1016/j.quascirev.2024.108992.

References

Ashok, K., Behera, S.K., Rao, S.A., Weng, H., Yamagata, T., 2007. El Niño modoki and its possible teleconnection. J. Geophys. Res. 112, C11007. https://doi.org/10.1029/2006JC003798.

Bard, E., Tuna, T., Fagault, Y., Bonvalot, L., Wacker, L., Fahrni, S., Synal, H.A., 2015. AixMICADAS, the accelerator mass spectrometer dedicated to ^{14}C recently installed in Aix-en-Provence, France. Nucl. Instrum. Methods Phys. Res. Sect. B Beam Interact. Mater. Atoms 361, 80–86.

Benallack, K., Green, A.N., Humphries, M.S., Cooper, J.A.G., Dladla, N.N., Finch, J.M., 2016. The stratigraphic evolution of a large back-barrier lagoon system with a non-migrating barrier. Mar. Geol. 379, 64–77.

Blaauw, M., Christen, J.A., 2011. Flexible paleoclimate age-depth models using an autoregressive gamma process. Bayesian Analysis 6, 457–474.

Blamey, R.C., Reason, C.J.C., 2023. Diversity and Ranking of ENSO Impacts along the Eastern Seaboard of Subtropical Southern Africa. Atmosphere 14, 1042.

Blamey, R.C., Kolusu, S.R., Mahlalela, P., Todd, M.C., Reason, C.J.C., 2018. The role of regional circulation features in regulating El Niño climate impacts over southern Africa: a comparison of the 2015/2016 drought with previous events. Int. J. Climatol. 38, 4276–4295.

Botha, G.A., Haldorsen, S., Porat, N., 2013. Geological history. In: Perissinotto, R., Stretch, D.D., Taylor, R.H. (Eds.), Ecology and Conservation of Estuarine Ecosystems: Lake St Lucia as a Global Model. Cambridge University Press, Cape Town, pp. 47–61.

Cao, H., Wang, Z., He, J., Guo, J., Jull, A.J.T., Zhou, A., Dong, G., Chen, F., 2023. Performance and inter-comparison tests of the MICADAS at the radiocarbon laboratory of Lanzhou University, China. Radiocarbon 65, 41–50.

Capotondi, A., Wittenburg, A.T., Newman, M., Di Lorenzo, W., Yu, J-Y., Braconnot, P., Cole, J., Dewitte, B., Giese, B., Guilyardi, E., Jin, F-F., Karnauskas, K., Kirtman, B., Lee, T., Schneider, N., Xue, Y., Yeh, S-W., 2015. Understanding ENSO diversity. Bull. Am. Meteorol. Soc. 96, 921–938. https://doi.org/10.1175/BAMS-D-13-00117.1.

Emile-Geay, J., Tingley, M., 2016. Inferring climate variability from nonlinear proxies: application to palaeo-ENSO studies. Clim. Past 12, 31–50.

Emile-Geay, J., Cobb, K.M., Cole, J.E., Elliot, M., Zhu, F., 2020. Past ENSO variability: reconstructions, models, and implications. In: McPhaden, M.J., Santoso, A., Cai, W. (Eds.), El Niño Southern Oscillation in a Changing Climate, pp. 87–118. https://doi.org/10.1002/9781119548164.ch5.

Hagemans, K., Nooren, K., de Haas, T., Córdova, M., Hennekam, R., Stekelenburg, M.C.A., Rodbell, D.T., Middelkoop, H., Donders, T.H., 2021. Patterns of alluvial deposition in Andean lake consistent with ENSO trigger. Quat. Sci. Rev. 259, 106900.

Hao, Y., Hao, Z., Feng, S., Zhang, X., Hao, F., 2020. Response of vegetation to El Niño-Southern Oscillation (ENSO) via compound dry and hot events in southern Africa. Global Planet. Change 195, 103358.

Hart, N.C.G., C.G, N., Reason, C.J.C., Fauchereau, N., 2010. Tropical-extratropical interactions over southern Africa: three cases of heavy summer season rainfall. Mon. Weather Rev. 138, 2608–2623.

Hart, N.C.G., Washington, R., Reason, C.J.C., 2018. On the likelihood of tropical-extratropical cloud bands in the South Indian Convergence Zone during ENSO events. J. Clim. 31, 2797–2817.

Hoell, A., Cheng, L., 2018. Austral summer Southern African precipitation extremes forced by the El Niño-Southern oscillation and the subtropical Indian Ocean dipole. Clim. Dynam. 50, 3219–3236.

Hoell, A., Funk, C., Zinke, J., Harrison, L., 2017. Modulation of the southern Africa precipitation response to the El Niño southern oscillation by the subtropical Indian Ocean Dipole. Clim. Dynam. 48, 2529–2540.

Hogg, A.G., Heaton, T.J., Hua, Q., Palmer, J.G., Turney, C.S.M., Southon, J., Bayliss, A., Blackwell, P.G., Boswijk, G., Bronk Ramsey, C., Pearson, C., Petchey, F., Reimer, P., Reimer, R., Wacker, L., 2020. SHCal20 southern hemisphere calibration, 0–55,000 Years cal BP. Radiocarbon 62, 759–778.

Humphries, M.S., Benitez-Nelson, C.R., Bizimis, M., Finch, J.M., 2017. An aeolian sediment reconstruction of regional wind intensity and links to larger scale climate variability since the last deglaciation from the east coast of southern Africa. Glob. Planet. Change 156, 59–67.

Humphries, M.S., Green, A.N., Finch, J.M., 2016. Evidence of El Niño driven desiccation cycles in a shallow estuarine lake: the evolution and fate of Africa's largest estuarine system, Lake St Lucia. Global Planet. Change 147, 97–105.

Humphries, M.S., Kirsten, K.L., McCarthy, T.S., 2019. Rapid changes in the hydroclimate of southeast Africa during the mid- to late-Holocene. Quat. Sci. Rev. 212, 178–186.

Humphries, M., Green, A., Higgs, C., Strachan, K., Hahn, A., Pillay, L., Zabel, M., 2020. High-resolution geochemical records of extreme drought in southeastern Africa during the past 7000 years. Quat. Sci. Rev. 236, 106294.

Jiménez-Muñoz, J.C., Mattar, C., Barichivich, J., Santamaría-Artigas, A., Takahashi, K., Malhi, Y., Sobrino, J.A., van der Schrier, G., 2016. Record-breaking warming and extreme drought in the Amazon rainforest during the course of El Niño 2015–2016. Sci. Rep. 6, 33130.

Jury, M.R., Nassor, A., Parker, B.A., Raholijao, N., 1995. Variability of summer rainfall over Madagascar: climatic determinants at interannual scales. Int. J. Climatol. 15, 1323–1332.

Karamperidou, C., DiNezio, P.N., 2022. Holocene hydroclimatic variability in the tropical Pacific explained by changing ENSO diversity. Nat. Commun. 13, 7244.

Karamperidou, C., Di Nezio, P.N., Timmermann, A., Jin, F.-F., Cobb, K.M., 2015. The response of ENSO flavors to mid-Holocene climate: implications for proxy interpretation. Paleoceanography 30, 527–547.

Kiefer, J., Karamperidou, C., 2019. High-resolution modeling of ENSO-induced precipitation in the tropical andes: implications for proxy interpretation. Paleoceanogr. Paleoclimatol. 34, 217–236.

Lazenby, M.J., Todd, M.C., Wang, Y., 2016. Climate model simulation of the South Indian Ocean Convergence Zone: mean state and variability. Clim. Res. 68, 59–71.

Lindesay, J.A., 1988. South African rainfall, the southern oscillation and a southern hemisphere semi-annual cycle. J. Climatol. 8, 17–30.

Malherbe, J., Dieppois, B., Maluleke, P., Van Staden, M., Pillay, D.L., 2016. South African droughts and decadal variability. Nat. Hazards 80, 657–681.

Manhique, A.J., Reason, C.J.C., Rydberg, L., Fauchereau, N., 2011. ENSO and Indian Ocean sea surface temperatures and their relationships with tropical temperate troughs over Mozambique and the southwest Indian Ocean. Int. J. Climatol. 31, 1–13.

Mark, S.Z., Abbott, M.B., Rodbell, D.T., Moy, C.M., 2022. XRF analysis of Laguna Pallcacocha sediments yields new insights into Holocene El Niño development. Earth Planet Sci. Lett. 593, 117657.

Mathivha, F.I., Mabala, L., Matimolane, S., Mbatha, N., 2024. El niño-induced drought impacts on reservoir water resources in South Africa. Atmosphere 15, 249.

Miller, C., Finch, J., Hill, T., Peterse, F., Humphries, M., Zabel, M., Schefuß, E., 2019. Late Quaternary climate variability at Mfabeni peatland, eastern South Africa. Clim. Past 15, 1153–1170.

Miller, C., Hahn, A., Liebrand, D., Zabel, M., Schefuβ, E., 2020. Mid- and low latitude effects on eastern South African rainfall over the Holocene. Quat. Sci. Rev. 229, 106088.

Mollenhauer, G., Grotheer, H., Gentz, T., Bonk, E., Hefter, J., 2021. Standard operation procedures and performance of the MICADAS radiocarbon laboratory at Alfred Wegener Institute (AWI), Germany. Nucl. Instrum. Methods Phys. Res. B. 496, 45–51.

Moy, C.M., Seltzer, G.O., Rodbell, D.T., Anderson, D.M., 2002. Variability of El niño/southern oscillation activity at millennial timescales during the Holocene epoch. Nature 420, 162–165.

Philippon, N., Rouault, M., Richard, Y., Favre, A., 2012. The influence of ENSO on winter rainfall in South Africa. Int. J. Climatol. 32, 2333–2347.

Ramdhunee, D., 2024. Aspects of the Geology and Geomorphology of Lake Bhangazi North: A Paleo-Estuary to the Mkhuze River. Unpublished MSc Dissertation. University of KwaZulu-Natal, Westville.

Reason, C.J.C., 2002. Sensitivity of the southern African circulation to dipole sea-surface temperature patterns in the south Indian Ocean. Int. J. Climatol. 22, 377–393.

Reason, C.J.C., Rouault, M., 2002. ENSO-like decadal variability and South African rainfall. Geophys. Res. Lett. 29, 1638. https://doi.org/10.1029/2002GL014663.

Reason, C.J.C., Allan, R.J., Lindesay, J.A., Ansell, T.J., 2000. ENSO and climatic signals across the Indian Ocean Basin in the global context: part I, interannual composite patterns. Int. J. Climatol. 20, 1285–1327.

Rein, B., Lückge, A., Reinhardt, L., Sirocko, F., Wolf, A., Dullo, W.-C., 2005. El Niño variability off Peru during the last 20,000 years. Paleoceanogr. Paleoclimatol. 20, PA4003.

Scroxton, N., Burns, S.J., McGee, D., Godfrey, L.R., Ranivoharimanana, L., Faina, P., Tiger, B.H., 2023. Hydroclimate variability in the Madagascar and southeast african summer monsoons at the mid- to late-holocene transition. Quat. Sci. Rev. 300, 107874.

Vecchi, G.A., Wittenberg, A.T., 2010. El Niño and our future climate: where do we stand? WIREs Climate Change 1, 260–270. https://doi.org/10.1002/wcc.33.

Vicente-Serrano, S.M., López-Moreno, J.I., Gimeno, L., Nieto, R., Morán-Tejeda, E., Lorenzo-Lacruz, J., Beguería, S., Azorin-Molina, C., 2011. A multiscalar global evaluation of the impact of ENSO on droughts. J. Geophys. Res. Atmos. 116, D20109. https://doi.org/10.1029/2011JD016039.
Wacker, L., Němec, M., Bourquin, J., 2010. A revolutionary graphitization system: fully automated, compact and simple. Nucl. Instrum. Methods Phys. Res. Sect. B Beam Interact. Mater. Atoms 268, 931–934.
Wang, L., Brook, G.A., Burney, D.A., Voarintsoa, N.R.G., Liang, F., Cheng, H., Edwards, R.L., 2019. The African Humid Period, rapid climate change events, the timing of human colonization, and megafaunal extinctions in Madagascar during the Holocene: evidence from a 2m Anjohibe Cave stalagmite. Quat. Sci. Rev. 210, 136–153.
Ward, P.J., Jongman, B., Kummu, M., Dettinger, M.D., Weiland, F.C.S., Winsemius, H.C., 2014. Strong influence of El Niño Southern Oscillation on flood risk around the world. Proc. Natl. Acad. Sci. USA 111, 15659–15664.
Washington, R., Preston, A., 2006. Extreme wet years over southern Africa: role of Indian Ocean sea surface temperatures. J. Geophys. Res. 111, D15104.
Wright, I., 2002. Aspects of the Cenozoic Evolution of the Northern KwaZulu-Natal Coastal Plain, South Africa. Bulletin No. 132. Council for Geoscience, Pretoria.
Zhang, Z., Leduc, G., Sachs, J.P., 2014. El Niño evolution during the Holocene revealed by a biomarkers rain gauge in the Galápagos Islands. Earth Planet Sci. Lett. 404, 420–434.